

Supporting Information

Critical role of dissolved oxygen and iron-copper synergy in dual-metals/char catalyst system

Yang Luo ^{a, b}, Hong Li ^{a, c}, Hailan Yang ^{a, b}, Zhiming Yang ^{a, b}, Chuang Li ^{a, b}, Shaoheng Liu ^d,
Qiang Chen ^a, Weihua Xu ^a, Wei Zhang ^a, Xiaofei Tan ^{a, b, *}

^a *College of Environmental Science and Engineering, Hunan University and Key Laboratory of Environmental Biology and Pollution Control (Hunan University), Ministry of Education, Changsha 410082, PR China.*

^b *Shenzhen Research Institute of Hunan University, Shenzhen 518055, PR China.*

^c *College of Resources and Environment, University of Chinese Academy of Sciences, Beijing 101408, PR China.*

^d *College of Chemistry and Material Engineering, Hunan University of Arts and Science, Changde 415000, PR China.*

* Corresponding author: Email address: tanxf@hnu.edu.cn (Xiaofei Tan)

This supplementary material includes 10 Texts, 7 Tables, and 22 Figures.

List of Supporting Information

Text S1. Chemical reagents.

Text S2. Characterization methods.

Text S3. Quantification of ROSs

Text S4. Electrochemical tests.

Text S5. HPLC-MS methods.

Text S6. Density functional theory (DFT) calculation method.

Text S7. CIP removal under different reaction parameters.

Text S8. Desorption of CIP.

Text S9. Detection method of PMSO and PMSO₂.

Text S10. Detection of high-valent metal species.

Table S1. EDS parameters of Fe/Cu-BC.

Table S2. Porosity characterizations of Fe/Cu-BC.

Table S3. XPS parameters of Fe/Cu-BC.

Table S4. The content of Fe and Cu in Fe/Cu-BC determined by digestion treatment.

Table S5. Fukui index of CIP.

Table S6. The degradation intermediates of CIP.

Table S7. The performance comparison of recently reported materials in oxygen activation.

Figure S1. SEM images of Fe/Cu-BC.

Figure S2. Elemental mapping of Fe/Cu-BC.

Figure S3. HRTEM images of Fe/Cu-BC.

Figure S4. N₂ adsorption-desorption isotherm and pore size distribution of Fe/Cu-BC.

Figure S5. XPS survey spectrum of Fe/Cu-BC.

Figure S6. (a) the removal of different organic pollutants by Fe/Cu-BC and (b) corresponding pseudo-first order kinetics. Pseudo-first order kinetics of CIP removal in different systems: (c) different materials and (d) initial pH.

Figure S7. Effects of (a, b) Fe/Cu-BC dosage, (c, d) initial CIP concentration and (e, f) reaction temperature on CIP removal.

Figure S8. The Zeta potential of Fe/Cu-BC.

Figure S9. The total ion chromatograms of CIP solution at different reaction times (0 min and 20 min).

Figure S10. TOC removal efficiency by Fe/Cu-BC.

Figure S11. Pseudo-first order kinetics of CIP removal in quenching experiments.

Figure S12. (a) PMSO consumption and PMSO₂ generation in Fe/Cu-BC system; (b) UV-vis spectra of Cu(III)-periodate complex.

Figure S13. (a) The standard curve of the NBT absorbance versus NBT concentration; (b) The standard curve of the p-HBA peak area versus p-HBA concentration; (c) The standard curve of the H₂O₂ absorbance versus H₂O₂ concentration.

Figure S14. Quantitative detection of (a) •OH and (b) H₂O₂ in different systems.

Figure S15. (a) Time profiles of the FFA degradation by different materials; (b) Plots of $-\ln(C/C_0)$ versus time for FFA degradation.

Figure S16. The concentration of Cu(I) in Fe/Cu-BC system.

Figure S17. (a) CV curves and (b) LSV curves of low-temperature biochars.

Figure S18. Leached Fe and Cu ions in Fe/Cu-BC system at pH=3 and 5.

Figure S19. Pseudo-first order kinetics of CIP removal in different systems: (a) coexisting anions, (b) humic acids and (c) real water samples.

Figure S20. (a) CIP removal efficiency and (b) leached Fe and Cu ions of three cycles in Fe/Cu-BC system.

Figure S21. XRD patterns of raw and used Fe/Cu-BC.

Figure S22. Mass spectrometry of intermediates for CIP degradation process.

Text S1. Chemical reagents.

Potassium ferrate (K_2FeO_4) was purchased from Shanghai Macklin Biochemical Co., Ltd. Ciprofloxacin (CIP), enrofloxacin (ENR), norfloxacin (NOR), tetracycline (TC), humic acid (HA), Superoxide Dismutase (SOD), 2,2'-Bipyridyl (BPY), neocuproine were provided by Yien Chemical Technology Co., Ltd. (Shanghai, China). Cupric nitrate [$Cu(NO_3)_2$], sodium hydroxide (NaOH), hydrochloric acid (HCl), methylene blue (MB), sodium chloride (NaCl), sodium thiosulfate ($Na_2S_2O_3$), tert-butyl alcohol (TBA), Dimethyl sulfoxide (DMSO), L-histidine were bought from Sinopharm Chemical Reagent Co. All chemicals were analytically pure, and all solution were prepared using ultrapure water (UW, $18.25\text{ M}\Omega\text{ cm}^{-1}$).

Text S2. Characterization methods.

X-ray diffraction pattern was measured (XRD, BrukerAXS D8, Germany) in the range of $5\sim 90^\circ$ ($5^\circ/\text{min}$) to observe the crystal phases of biochar. The morphological and structural details and elemental compositions of biochar were characterized by scanning electronic microscopy with energy dispersive X-ray spectroscopy (SEM-EDS, ZEISS Sigma 500, Germany) and transmission electro-microscopy (TEM, FEI talos f200s). The surface functional groups were detected by Fourier transform infrared spectrometer in a region of $4000\text{-}400\text{ cm}^{-1}$ (FTIR, Thermo Scientific Nicolet iS5). The surface element contents and chemical states were investigated by X-ray photoelectron spectroscopy (XPS, Thermo ESCALAB 250Xi, USA). Raman spectra with the excitation wavelength at 532 nm (HORIBA HR Evolution) was analyzed the defect structure of biochar. The specific surface area (SSA) and pore size distribution of biochar were determined and calculated by the nitrogen adsorption-desorption method using the automatic surface area porosity analyzer (Micromeritics APSP 2460, USA).

Text S3. Quantification of ROSs

Quantification of $O_2^{\bullet-}$. Nitrotetrazolium blue chloride (NBT) was used as the molecular probe of $O_2^{\bullet-}$. It has a characteristic absorption wavelength of 260 nm and does not react with other ROS but $O_2^{\bullet-}$.¹ The yellow NBT was reduced to blue formazan by $O_2^{\bullet-}$. The concentration of $O_2^{\bullet-}$ could be calculated by Eq. S5:

$$\text{Cumulative } [O_2^{\bullet-}]_t = ([NBT]_0 - [NBT]_t) \times 4 \quad (\text{S5})$$

where the initial concentration of NBT is 0.1 mM. The concentration change of NBT was measured at 259 nm with UV-vis spectrophotometer.

Quantification of $\bullet OH$. Benzoic acid (BA) was employed as a probe molecule to quantify the formation of $\bullet OH$.² The products of BA reacts with $\bullet OH$ are p-hydroxybenzoic acid (p-HBA), m-HBA and o-HBA in a ratio of 1.2:2.3:1.7.³ The concentration of produced p-HBA is utilized to estimate $\bullet OH$ concentration with a conversion factor of 5.87. Thus, the concentration of $O_2^{\bullet-}$ could be calculated by Eq. S6:

$$\text{Cumulative } [\bullet OH] = [p\text{-HBA}] \times 5.87 \quad (\text{S6})$$

The p-HBA was determined by high performance liquid chromatography (HPLC, Agilent 1260, Germany) with C18 column (5 μm , 150 \times 4.6 mm). The mobile phase contained 40% methanol and 60% acetic acid (1%) with a flow rate of 1 mL/min. The injection volume was 10 μL and the detection wavelength was 254 nm.

Quantification of H_2O_2 . The concentration of H_2O_2 was tested by the iodometry method. In detail, 0.5 g/L Fe/Cu-BC sample was added to 50 mL ultrapure water. At given time intervals, 1 mL of the liquid sample was sampled and filtrated through 0.22 μm membranes. Then, 1 mL liquid sample was mixed with 1 mL potassium hydrogen phthalate solution (0.1 M) and 1mL

KI solution (0.4 M). The reaction solution was measured by an UV-Vis spectrophotometer, and the detection peak of H₂O₂ is 350 nm.

Quantification of ¹O₂. The amount of ¹O₂ was quantified by monitoring the decrease of furfuryl alcohol (FFA), which is usually used as a probe molecule to identify ¹O₂ due to their highly specific reaction.⁴ The reaction rate between FFA and ¹O₂ could be shown as Eqs. (S7-S9):

$$-\frac{d[\text{FFA}]}{dt} = k_{\text{FFA}} [{}^1\text{O}_2] [\text{FFA}] \quad (\text{S7})$$

$$-\frac{d[\text{FFA}]}{dt} = k_{\text{FFA}} [{}^1\text{O}_2] [\text{FFA}] = k_{\text{ex}} [\text{FFA}] \quad (\text{S8})$$

$$[{}^1\text{O}_2]_{\text{ss}} = \frac{k_{\text{ex}}}{k_{\text{FFA}}} \quad (\text{S9})$$

where k_{ex} is the experimentally measured quasi-first order rate of FFA degradation. Thus, the steady-state concentration of ¹O₂ could be calculated based on eq 9. The k_{FFA} value is $1.2 \times 10^8 \text{ mol}^{-1} \text{ s}^{-1}$. The concentration variation of FFA was monitored by high performance liquid chromatography (HPLC, Agilent 1260, Germany) with C18 column (5 μm, 150 × 4.6 mm). The eluent contained acetic acid (0.75%) and acetonitrile with a volum ratio of 70:30. The flow rate of HPLC is 1 mL/min. The UV detector was set at 275 nm and the column temperature was maintained at 35°C.

Text S4. Electrochemical tests.

Electrochemical measurements including cyclic voltammetry (CV) and linear sweep voltammetry (LSV) were measured by a CHI 660D workstation. In detail, glassy carbon electrodes (GCEs) loaded with four materials were first prepared, respectively. BC, Fe-BC, Cu-

BC or Fe/Cu-BC (2 mg), was dispersed into naphthol-ethyl alcohol solution (1:19, v: v) with 0.5 h ultrasonic treatment. Then, the mixed suspension was dropped onto the surface of GCEs and the above steps were repeated three times. Subsequently, the GCEs were dried at 60°C for 1 h. The electrochemical measurements were performed by the electrochemical workstation (CHI 660D). The cell system contained an electrolyte of 0.2 M Na₂SO₄ solution. The electrochemical measurement was conducted in a three-electrode cell with Pt electrode as counter electrode and Ag/AgCl electrode as the reference electrode.

Text S5. HPLC-MS methods

Intermediate products were analyzed by the ultra-high-performance liquid chromatography (Agilent 1290) coupled with the mass spectrometer (Agilent q-ToF 655). The flow rate was set to 0.3 mL/min and the injection volume was 5 µL. The chromatographic column was waters BEH C18 (1.7 µm, 2.1 mm × 100 mm). The mobile phases consisted of 0.1% formic acid (A) and acetonitrile (B). MS analyses was operated in ESI mode using Jetstream positive ionization over a mass scan range of 50-1000 m/z. The ionization source conditions used were as follows: sheath gas 12 L/min; sheath gas temperature was 350°C and the capillary voltage 4000 V.

Text S6. Density functional theory (DFT) calculation method.

DFT calculations were conducted using Gaussian 16 package. B3LYP functional with the 6-311G (2d, p) basis set was used for geometry optimization, electronic static potential (ESP), and frontier molecular orbital analysis (LUMO, HOMO). Solvation (water) model was adopted. Weak interaction was not considered. Fukui function is an important concept in conceptual

density functional theory, which has been widely used to predict reaction sites.⁵ B3LYP functional with the 6-311G (2d, p) basis set was utilized for Fukui index analysis (f^+ , f^- , f^0 and condensed dual descriptor (CDD)). The expression of Fukui function was shown in Eq. (S1), and the condensed Fukui function can be calculated by Eqs. (S2-S4).^{6,7}

$$f(r) = \left[\frac{\partial \rho(r)}{\partial N} \right]_{V(r)} \quad (\text{S1})$$

$$\text{Nucleophilic attack: } f^+(r) = \rho_{N+1}(r) - \rho_N(r) \quad (\text{S2})$$

$$\text{Electrophilic attack: } f^-(r) = \rho_N(r) - \rho_{N-1}(r) \quad (\text{S3})$$

$$\text{Radical attack: } f^0(r) = \frac{f^+(r) + f^-(r)}{2} = \frac{\rho_{N+1}(r) - \rho_{N-1}(r)}{2} \quad (\text{S4})$$

where N is number of electrons in present system, the constant term v in the partial derivative is external potential, and $\rho(r)$ is the electron density at a point r in space.

Text S7. CIP removal under different reaction parameters.

Some critical reaction parameters have significant effects on the removal efficiency of pollutants. Figure S7a shows the effect of Fe/Cu-BC dosage on CIP removal. Overall, CIP removal rate was positively correlated with the material dosage. When Fe/Cu-BC dosage increased from 0.1 g/L to 0.7 g/L, the removal of CIP rapidly improved from 55.57% to 93.75%, and the corresponding k_{obs} also improved from 0.011 min⁻¹ to 0.043 min⁻¹. It is well known that a higher catalyst dosage can provide more active sites, which is responsible for this outcome. However, when the amount of material increased from 0.5 g/L to 0.7 g/L, CIP removal was only a slight increase of 0.98%. Therefore, 0.5 g/L was chosen as the optimum material dosage in this study from an economic perspective while ensuring removal efficiency. The influence of initial CIP concentration on its removal was investigated in the range of 5 ~ 30 mg/L, as

shown in Figure S7c. At the initial CIP concentrations of 5, 10, 20 and 30 mg/L, the CIP removal efficiency within 90 min were reached 93.21%, 92.77%, 89.22% and 87.6%, and the corresponding k_{obs} was 0.037 min⁻¹, 0.033 min⁻¹, 0.029 min⁻¹ and 0.026 min⁻¹, respectively. This result indicated that CIP removal by Fe/Cu-BC decreased slowly as CIP concentration increased, which may be related to the competition between excess contaminants and a limited number of reactive sites. Figure S7e presents the removal of CIP using Fe/Cu-BC at different reaction temperatures (5, 15, 25 and 35°C). It was evident that a higher reaction temperature could accelerate CIP elimination, and k_{obs} increased obviously from 0.026 min⁻¹ at 5°C to 0.044 min⁻¹ at 35°C, which suggested that the removal of CIP by Fe/Cu-BC was an endothermic reaction.

Text S8. Desorption of CIP.

Desorption experiments were performed using ethanol extraction. First, solid-liquid separation was performed on the solution at the end of the reaction. The used Fe/Cu-BC was placed in 50 mL absolute ethanol and shaken for 24 h, and 1 mL of sample was taken out at 0.2, 0.5, 1, 2, 4, 7, 10, and 24 h for determination of CIP concentration.

Text S9. Quantification method of PMSO and PMSO₂.

The concentration of PMSO and PMSO₂ was measured by high performance liquid chromatography (HPLC, Agilent 1260, Germany) with C18 column (5 μm, 250 × 4.6 mm). The mobile phase was water and acetonitrile at a volume ratio of 80:20. The injection volume was 10 μL and the flow rate was 1 mL/min. The test was performed in UV mode at 215 nm.

Text S10. Detection of high-valent metal species.

The possible role of high-valent metal species in the system was considered, such as Fe(IV) and Cu(III), which efficiently degrade contaminants through non-radical pathways.^{8, 9} A number of researchers have reported that the Fenton reaction of Fe(II) with H₂O₂ readily to create Fe(IV) at near-neutral pH.¹⁰ PMSO was selected as a probe to verify the presence of Fe(IV). In general, PMSO consumption and PMSO₂ generation indicate the presence of Fe(IV).¹¹ The absence of PMSO₂ was observed in [Figure S12a](#), suggesting that no Fe(IV) was produced in the system. According to literature, Cu(III) can be formed through a two-electron transfer reaction between Cu(I) and H₂O₂, and Cu(III) produced by Fenton-like reaction appears to have higher reactivity than Fe(IV) produced under comparable condition.¹² The presence of Cu(III) was identified with periodate, which combines with Cu(III) to generate the stable Cu(III)-periodate complex featuring characteristic absorbance at 415 ± 5 nm.¹³ No distinct characteristic peaks were detected in [Figure S12b](#). Consequently, there were no high valence metals in Fe/Cu-BC system.

Table S1. EDS parameters of Fe/Cu-BC.

Material	Elements (wt%)					
	C	O	N	K	Fe	Cu
Fe/Cu-BC	69.66	26.06	1.27	7.66	2.37	2.86

Table S2 Porosity characterizations of Fe/Cu-BC.

Biochar	S_{BET} (m^2/g)	V_{total} (cm^3/g)	Ave-pore radius (nm)
Fe/Cu-BC	3.364	0.017	20.071

Table S3. XPS parameters of Fe/Cu-BC.

Material	Elements (wt%)					
	C	O	N	K	Fe	Cu
Fe/Cu-BC	53.50	28.32	2.60	12.92	0.73	1.93

Table S4. The content of Fe and Cu in Fe/Cu-BC determined by digestion treatment.

Material	Fe/Cu-BC	
Concentration (mg/kg)	Fe	90606.8
	Cu	98790.9
Mass fraction (wt%)	Fe	9.0607%
	Cu	9.8791%

Table S5. Fukui index of CIP.

Atom	q(N)	q(N+1)	q(N-1)	f ⁻	f ⁺	f ⁰	CDD
1(C)	0.0742	0.0412	0.1275	0.0533	0.033	0.0431	-0.0203
2(C)	-0.0378	-0.0812	-0.012	0.0258	0.0434	0.0346	0.0176
3(C)	-0.0341	-0.0412	0.0328	0.067	0.0071	0.037	-0.0599
4(C)	0.0417	0.0338	0.0682	0.0264	0.0079	0.0172	-0.0185
5(C)	-0.0816	-0.1159	-0.0528	0.0289	0.0343	0.0316	0.0054
6(C)	0.044	0.0142	0.0671	0.0231	0.0298	0.0264	0.0068
7(H)	0.0555	0.0293	0.0782	0.0227	0.0263	0.0245	0.0036
8(C)	0.103	0.0618	0.126	0.0231	0.0411	0.0321	0.018
9(H)	0.0299	0.0134	0.046	0.0161	0.0165	0.0163	0.0004
10(C)	0.0458	-0.0407	0.0648	0.019	0.0865	0.0527	0.0676
11(C)	-0.0582	-0.0894	-0.0355	0.0227	0.0312	0.0269	0.0085
12(H)	0.0512	0.0135	0.0672	0.016	0.0377	0.0268	0.0217
13(C)	0.1911	0.1673	0.2014	0.0103	0.0238	0.017	0.0135
14(O)	-0.3096	-0.3479	-0.2753	0.0344	0.0383	0.0363	0.0039
15(O)	-0.1576	-0.1781	-0.1476	0.01	0.0205	0.0152	0.0105
16(H)	0.17	0.1459	0.1875	0.0176	0.0241	0.0208	0.0066
17(C)	0.0221	0.016	0.021	-0.001	0.006	0.0025	0.007
18(C)	-0.062	-0.0766	-0.0549	0.0071	0.0146	0.0108	0.0075
19(C)	-0.0557	-0.071	-0.041	0.0147	0.0153	0.015	0.0006
20(H)	0.0465	0.0058	0.0551	0.0086	0.0406	0.0246	0.032
21(H)	0.0448	0.0168	0.0537	0.009	0.0279	0.0185	0.019
22(H)	0.0483	0.039	0.0521	0.0038	0.0093	0.0065	0.0055
23(H)	0.0501	0.026	0.0651	0.0151	0.0241	0.0196	0.009
24(H)	0.0526	0.0412	0.0616	0.009	0.0114	0.0102	0.0024
25(N)	0.0101	-0.0119	0.0262	0.0161	0.022	0.0191	0.006
26(N)	-0.0441	-0.0554	0.0426	0.0867	0.0113	0.049	-0.0754
27(C)	-0.0035	-0.0115	0.0132	0.0166	0.008	0.0123	-0.0086
28(C)	-0.0015	-0.0092	0.013	0.0144	0.0078	0.0111	-0.0067
29(C)	-0.0099	-0.0187	0.0045	0.0144	0.0088	0.0116	-0.0056
30(H)	0.037	0.0296	0.0505	0.0135	0.0074	0.0105	-0.0061
31(C)	-0.0099	-0.0229	0.0023	0.0122	0.013	0.0126	0.0008
32(H)	0.0248	0.0092	0.0523	0.0275	0.0156	0.0216	-0.0119
33(N)	-0.1514	-0.1578	-0.1228	0.0287	0.0064	0.0175	-0.0223
34(H)	0.0232	-0.0011	0.0457	0.0225	0.0243	0.0234	0.0018
35(H)	0.016	-0.0077	0.0346	0.0186	0.0237	0.0212	0.0051
36(F)	-0.0949	-0.1205	-0.0563	0.0386	0.0256	0.0321	-0.013
37(H)	0.0986	0.0666	0.1233	0.0248	0.032	0.0284	0.0072
38(H)	0.032	0.0215	0.0496	0.0176	0.0106	0.0141	-0.007
39(H)	0.0243	0.0032	0.0565	0.0323	0.021	0.0266	-0.0112
40(H)	0.0399	0.0114	0.0601	0.0201	0.0286	0.0244	0.0084
41(H)	0.0336	0.0195	0.055	0.0215	0.014	0.0178	-0.0074
42(O)	-0.2975	-0.3638	-0.2061	0.0914	0.0663	0.0788	-0.0251

Table S6. The degradation intermediates of CIP.

Compound	Molecular formula	m/z	Molecular structure
P1	$C_{17}H_{26}FN_3O_3$	340	
P2	$C_{17}H_{18}FN_3O_4$	348	
P3	$C_{16}H_{18}FN_3O$	288	
P4	$C_{17}H_{16}FN_3O_5$	362	
P5	$C_{16}H_{18}FN_3O_3$	318	
P6	$C_{13}H_9FN_2O_5$	293	
P7	$C_{13}H_{11}FN_2O_3$	263	

P8

$C_{12}H_{12}N_2O_3$

233

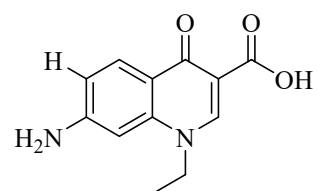


Table S7. The performance comparison of recently reported materials in oxygen activation.

Material dosage (g/L)	Contaminant (mg/L)	C/C ₀ (%)	Reaction	Ref.
			time (min)	
Fe/Cu-BC (0.5)	CIP (10)	94.8	90	This work
Cu/Fe@zeolite (2.0)	BPA (10)	87	120	14
CuCoFe-300 (2.0)	CIP (15)	82.5	250	1
BC-FexPCu (5.0)	TCPA (10)	100	240	15
C3N4-NDCN (1.0)	SMX (5)	95.3	240	16
Cu ⁰ /C (1.0)	SMT (20)	98.4	90	13
BC-FeCu (0.05)	TC (10)	92.5	360	17

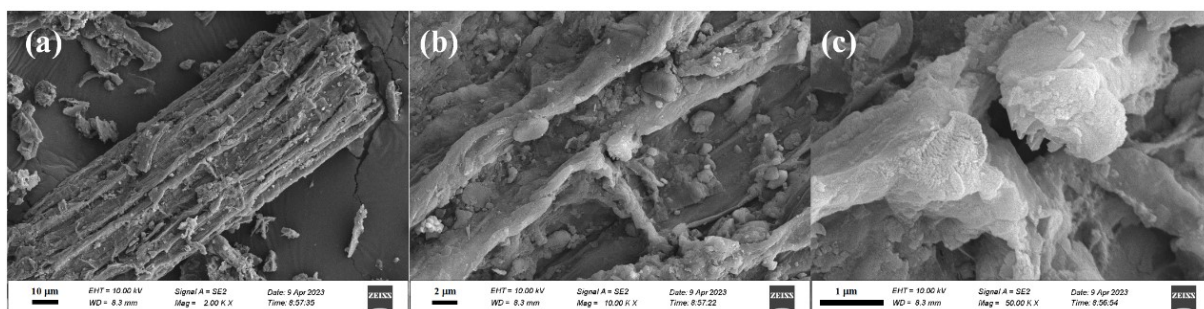


Figure S1. SEM images of Fe/Cu-BC.

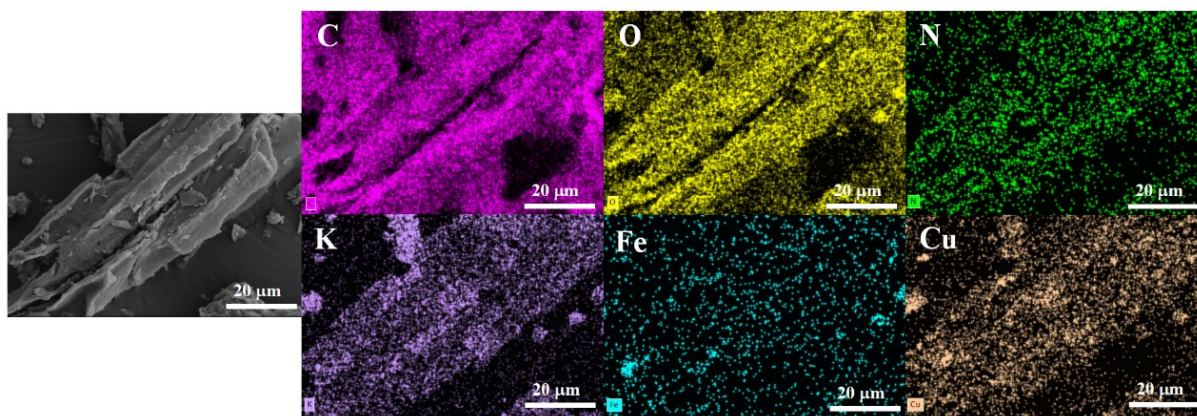


Figure S2. Elemental mapping of Fe/Cu-BC.

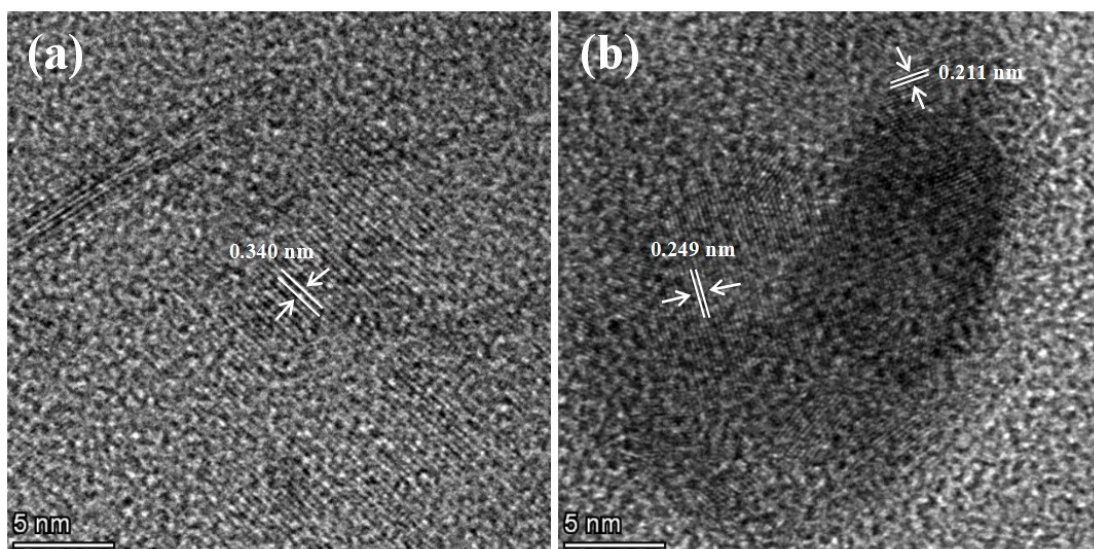


Figure S3. HRTEM images of Fe/Cu-BC.

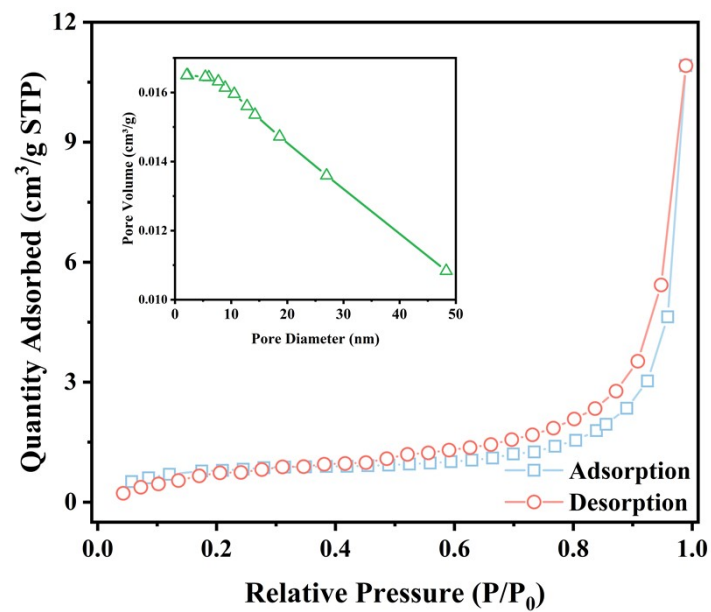


Figure S4. N₂ adsorption-desorption isotherm and pore size distribution of Fe/Cu-BC.

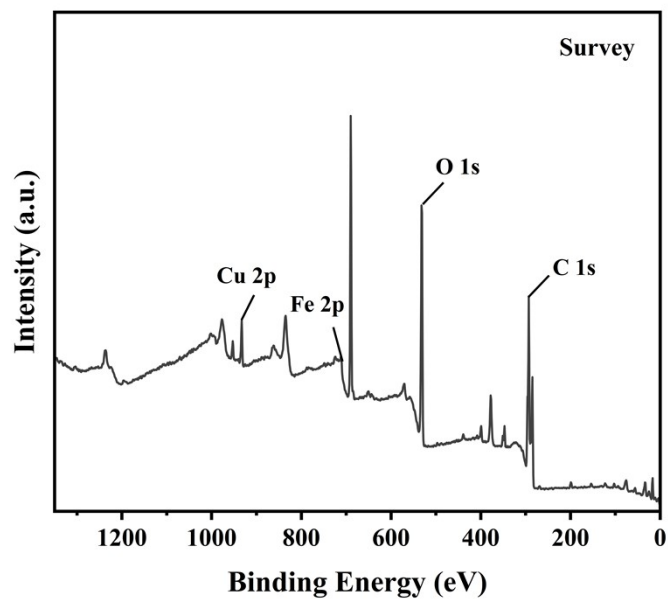


Figure S5. XPS survey spectrum of Fe/Cu-BC.

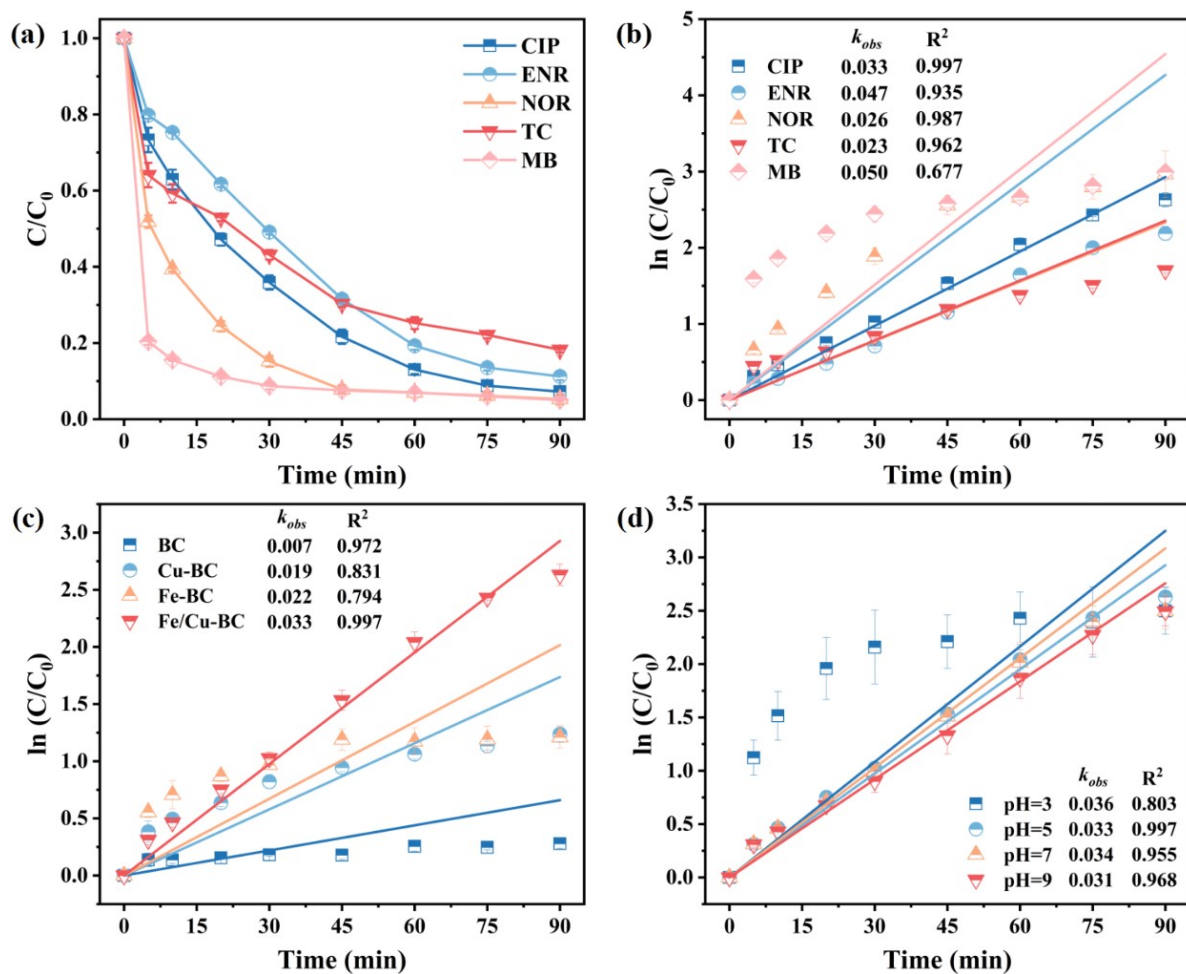


Figure S6. (a) the removal of different organic pollutants by Fe/Cu-BC and (b) corresponding pseudo-first order kinetics. Pseudo-first order kinetics of CIP removal in different systems: (c) different materials and (d) initial pH. Conditions: [CIP] = 10 mg/L, [ENR] = 10 mg/L, [NOR] = 10 mg/L, [TC] = 10 mg/L, [MB] = 10 mg/L, [biochar] = 0.5 g/L, [temperature] = 25°C.

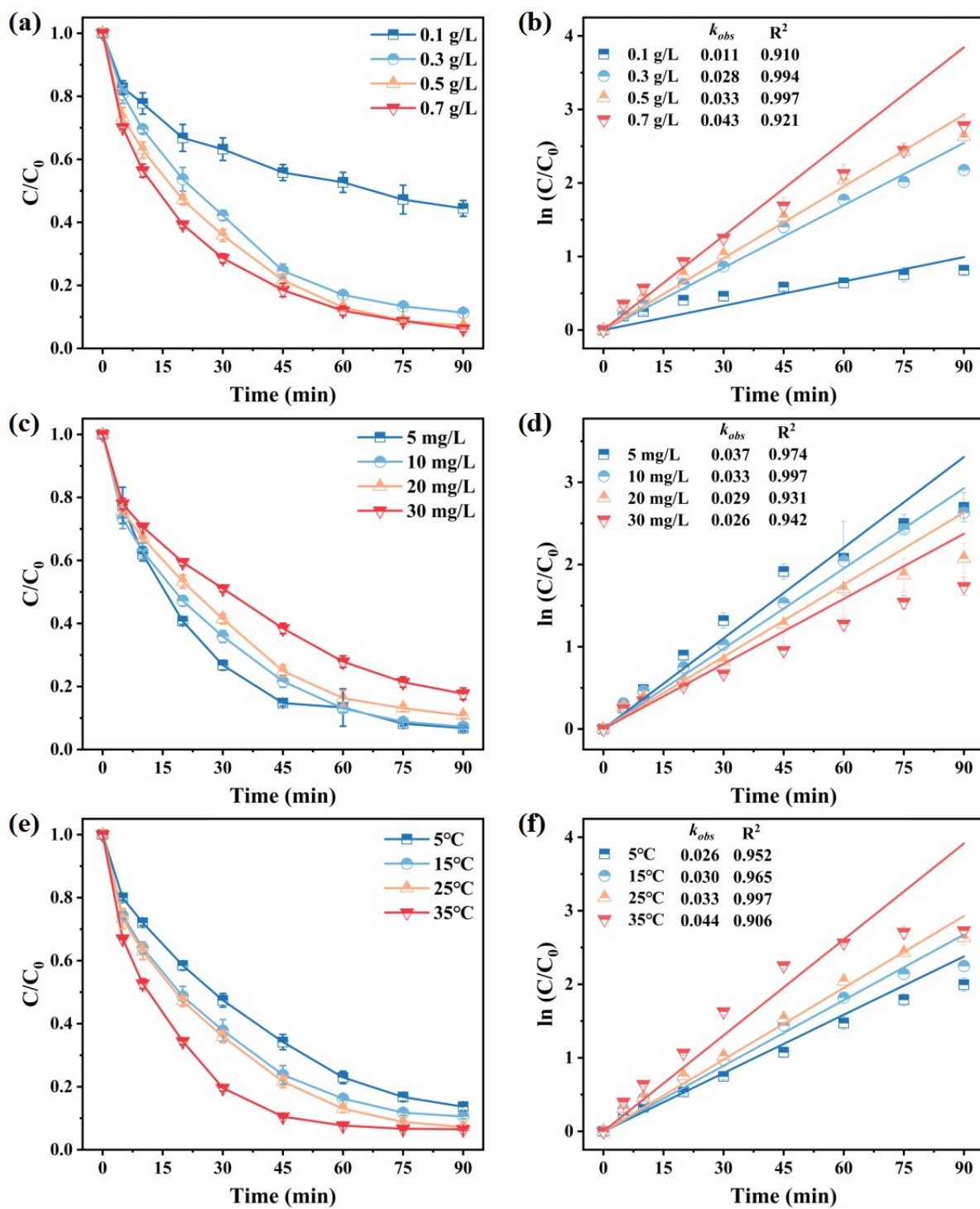


Figure S7. Effects of (a, b) Fe/Cu-BC dosage, (c, d) initial CIP concentration and (e, f) reaction temperature on CIP removal.

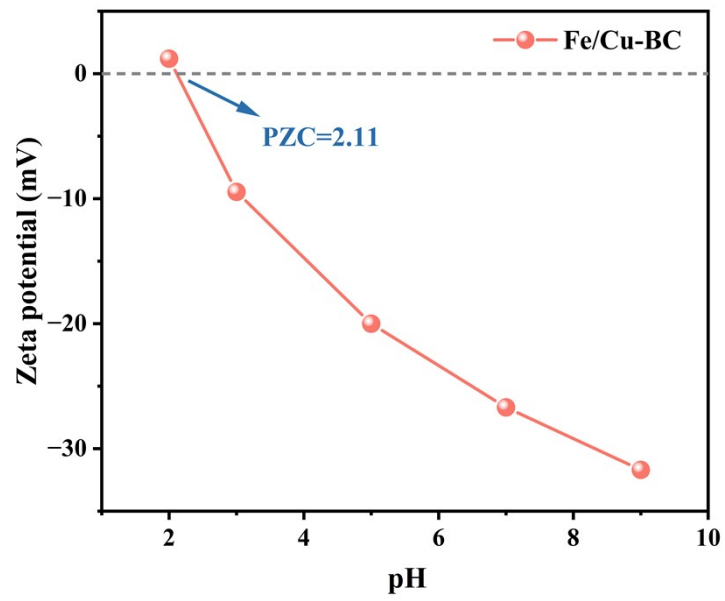


Figure S8. The Zeta potential of Fe/Cu-BC

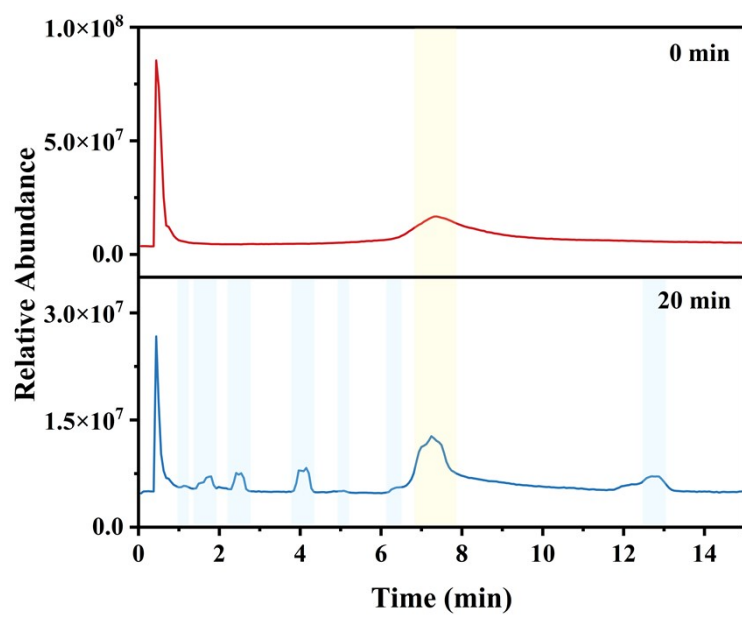


Figure S9. The total ion chromatograms of CIP solution at different reaction times (0 min and 20 min).

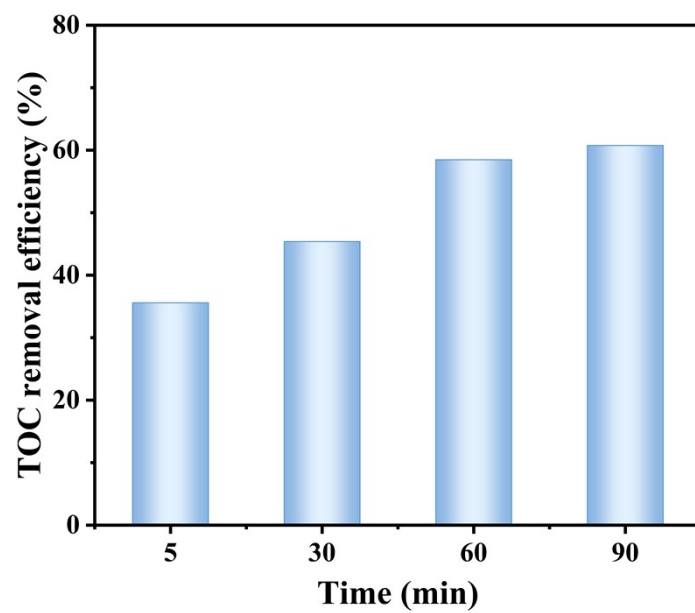


Figure S10. TOC removal efficiency by Fe/Cu-BC.

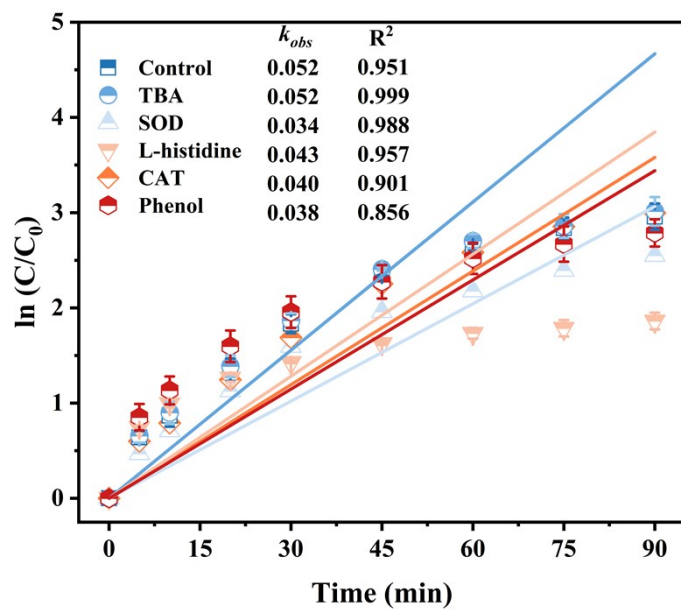


Figure S11. Pseudo-first order kinetics of CIP removal in quenching experiments.

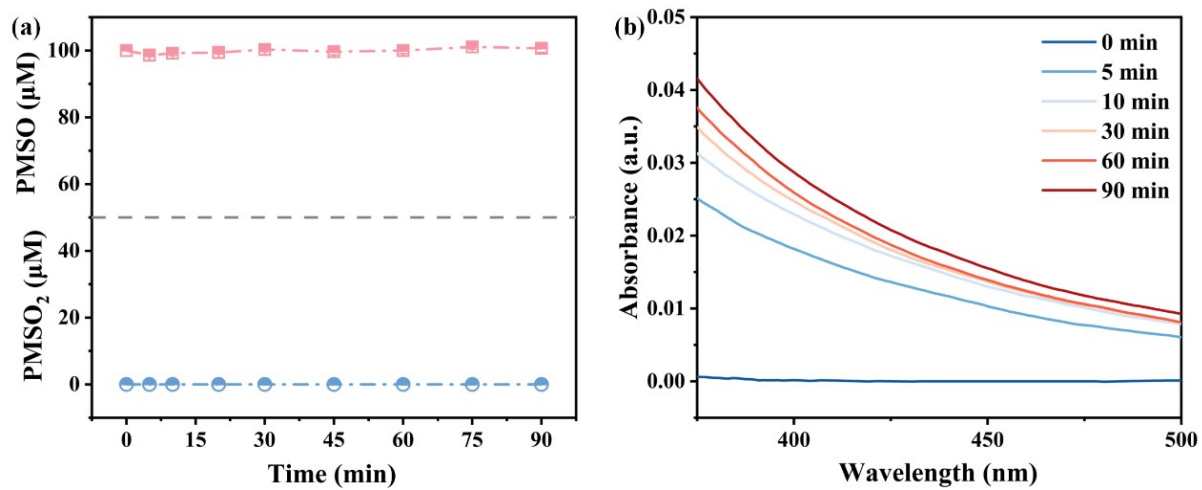


Figure S12. (a) PMSO consumption and PMSO₂ generation in Fe/Cu-BC system; (b) UV-vis spectra of Cu(III)-periodate complex.

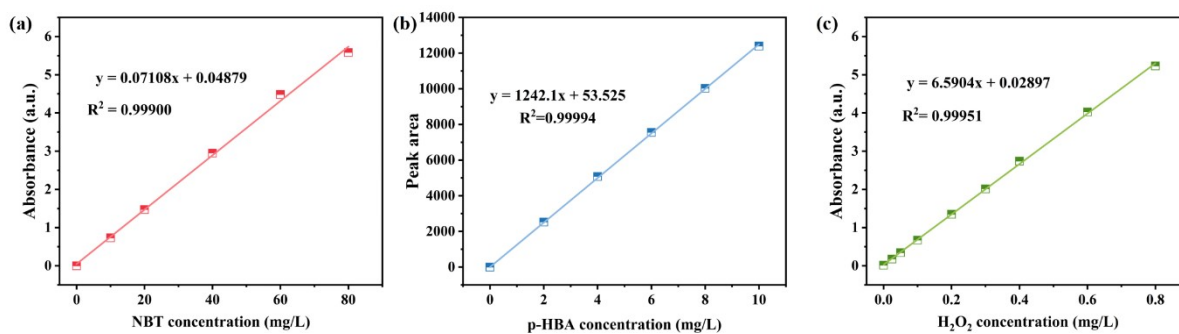


Figure S13. (a) The standard curve of the NBT absorbance versus NBT concentration; (b) The standard curve of the p-HBA peak area versus p-HBA concentration; (c) The standard curve of the H₂O₂ absorbance versus H₂O₂ concentration.

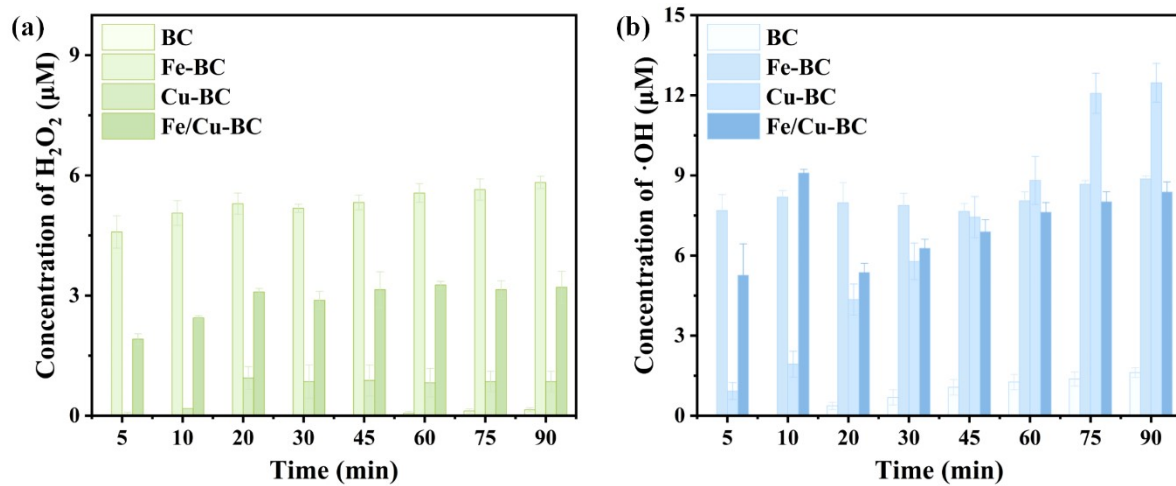


Figure S14. Quantitative detection of (a) •OH and (b) H₂O₂ in different systems. Conditions:

[biochar] = 0.5 g/L, [BA] = 10 mM.

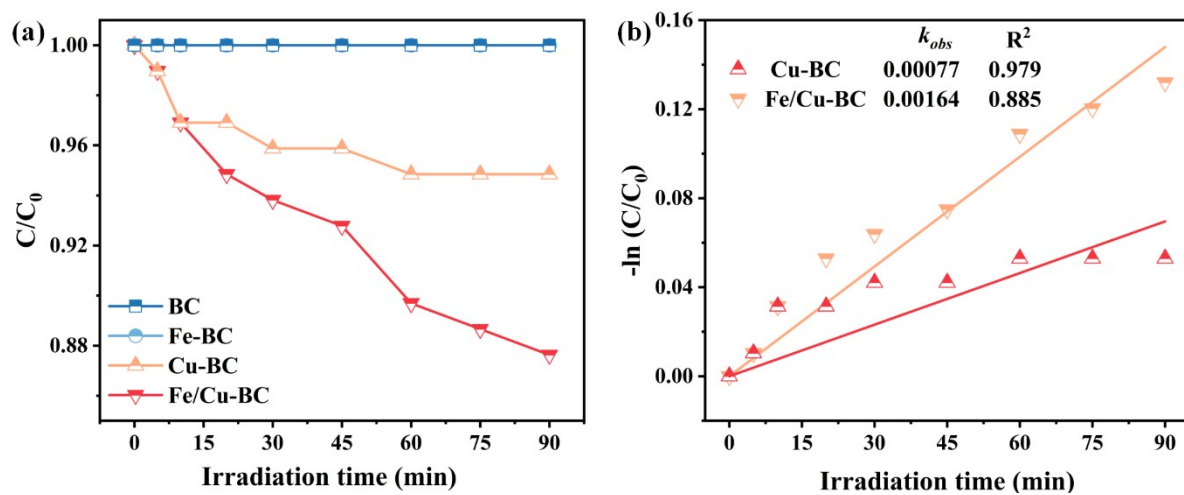


Figure S15. (a) Time profiles of the FFA degradation by different materials; (b) Plots of $-\ln(C/C_0)$ versus time for FFA degradation. Conditions: [biochar] = 0.5 g/L, [FFA] = 0.2 mM.

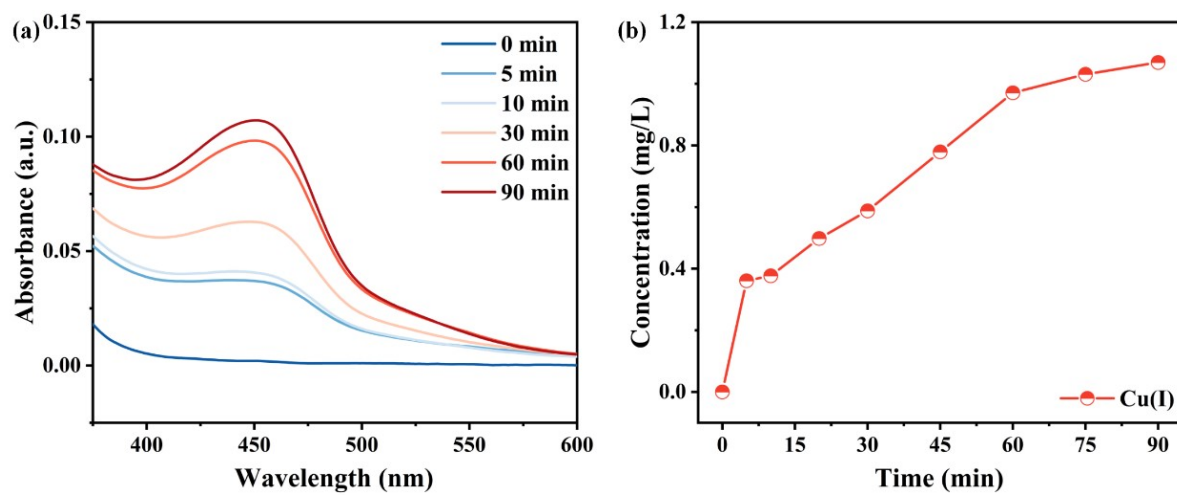


Figure S16. The concentration of Cu(I) in Fe/Cu-BC system.

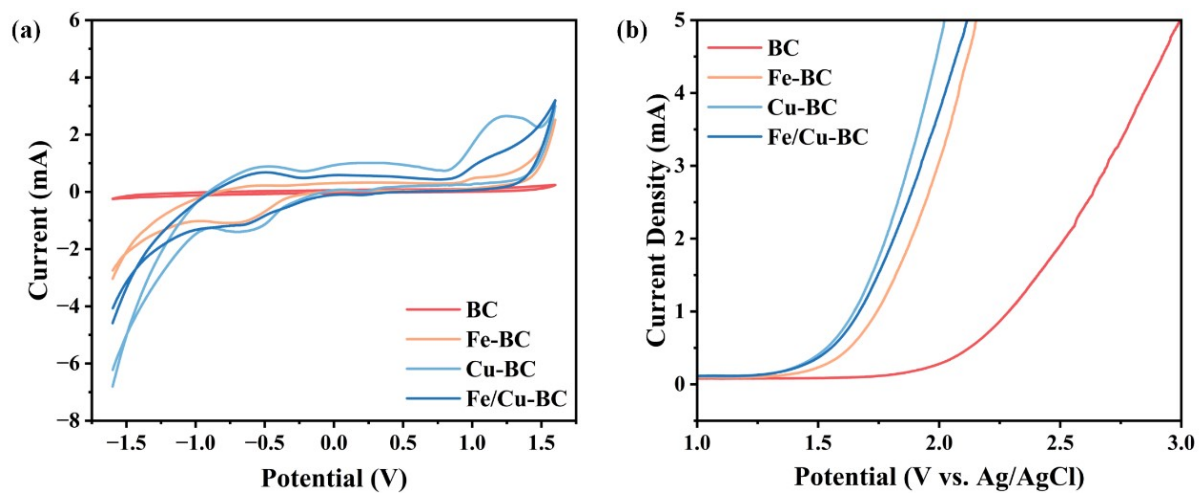


Figure S17. (a) CV curves and (b) LSV curves of low-temperature biochars.

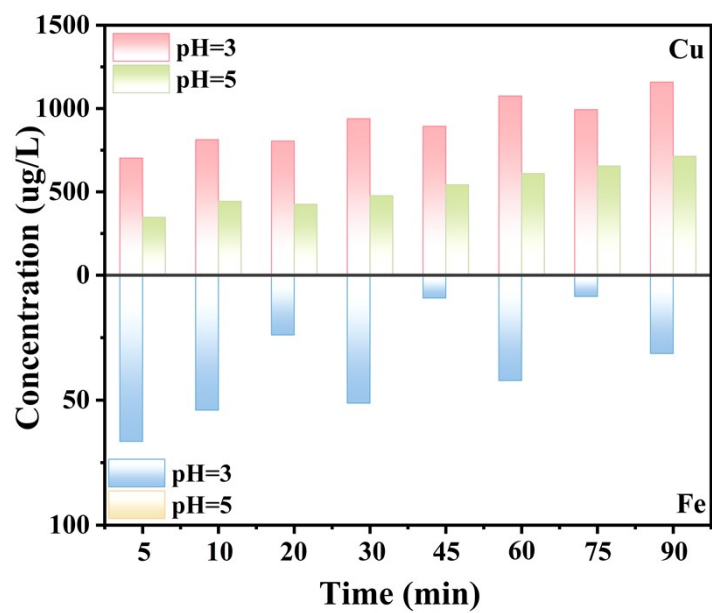


Figure S18. Leached Fe and Cu ions in Fe/Cu-BC system at pH=3 and 5.

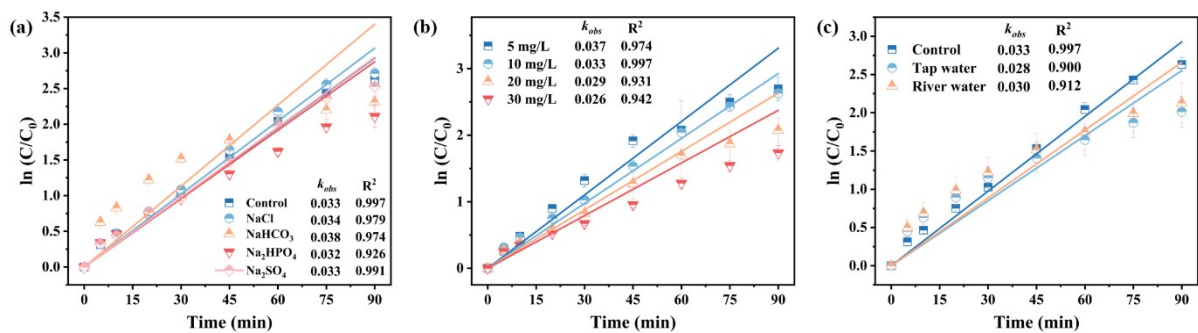


Figure S19. Pseudo-first order kinetics of CIP removal in different systems: (a) coexisting anions, (b) humic acids and (c) real water samples. Conditions: [CIP] = 10 mg/L, [biochar] = 0.5 g/L, [temperature] = 25°C.

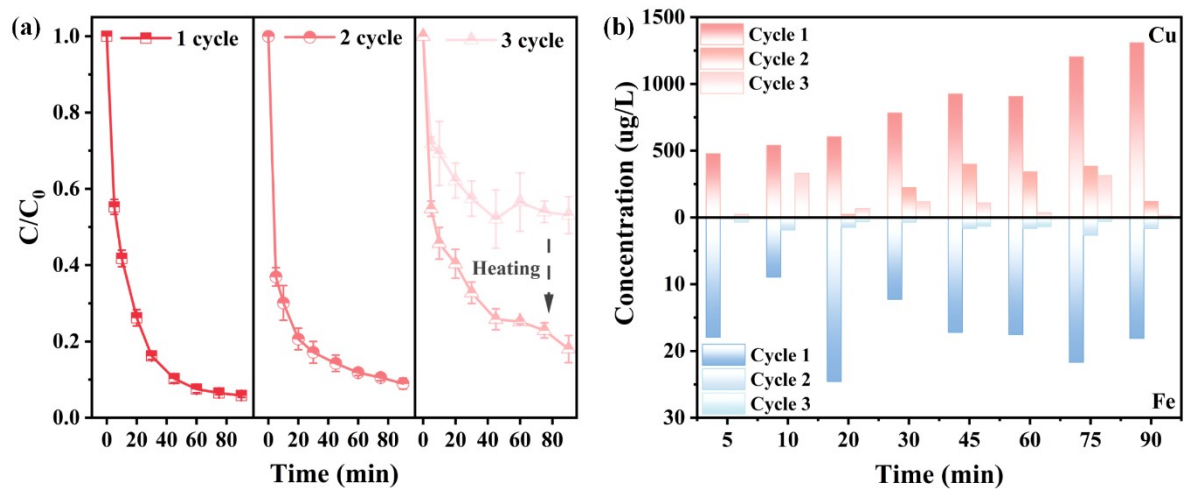


Figure S20. (a) CIP removal efficiency and (b) leached Fe and Cu ions of three cycles in Fe/Cu-BC system.

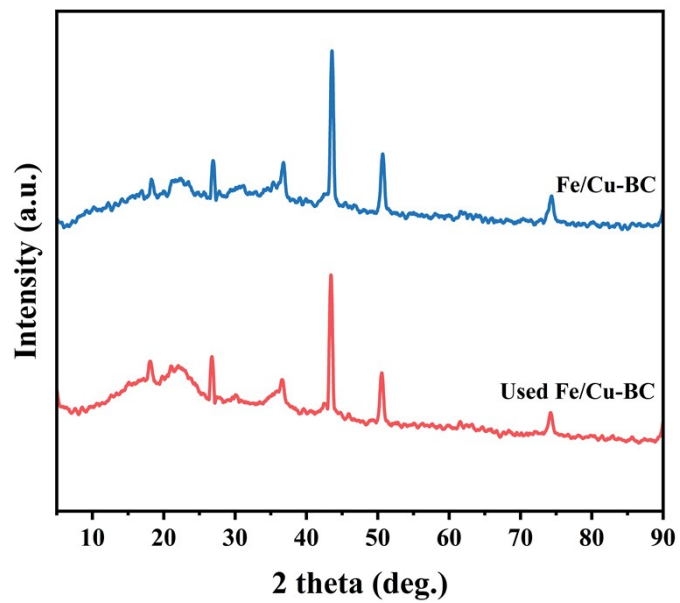


Figure S21. XRD patterns of raw and used Fe/Cu-BC.

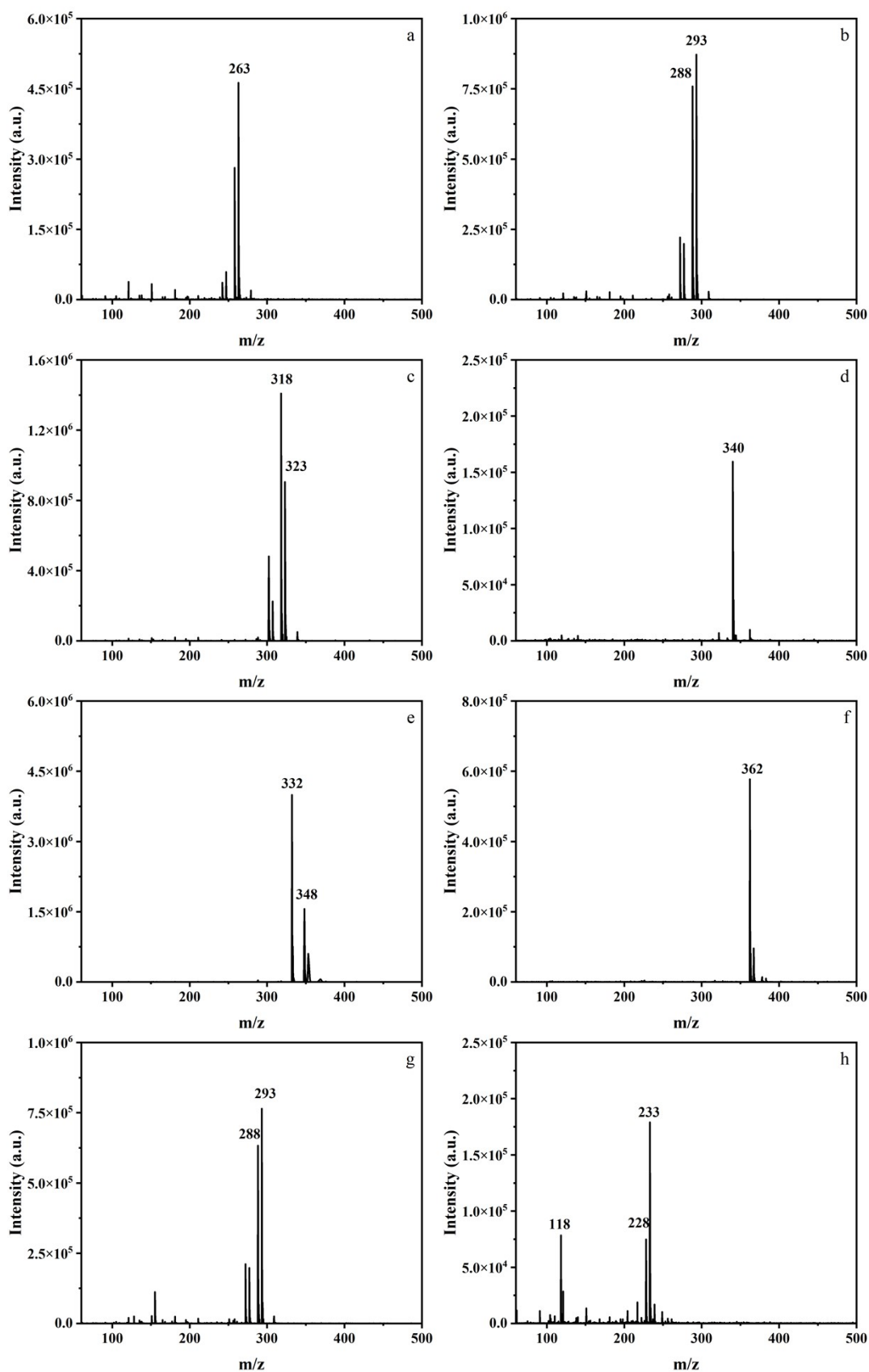


Figure S22. Mass spectrometry of intermediates for CIP degradation process.

Reference:

1. S. Wang, T. Li, X. Cheng, R. Zhu and Y. Xu, Regulating the concentration of dissolved oxygen to achieve the directional transformation of reactive oxygen species: A controllable oxidation process for ciprofloxacin degradation by calcined CuCoFe-LDH, *Water Research*, 2023, **233**.
2. N. Zheng, L. Li, X. Tang, W. Xie, Q. Zhu, X. Wang, Y. Lian, J. C. Yu and Z. Hu, Spontaneous Formation of Low Valence Copper on Red Phosphorus to Effectively Activate Molecular Oxygen for Advanced Oxidation Process, *Environmental Science & Technology*, 2023, **57**, 5024-5033.
3. Y. Mu, Z. Ai and L. Zhang, Phosphate Shifted Oxygen Reduction Pathway on Fe@Fe₂O₃ Core-Shell Nanowires for Enhanced Reactive Oxygen Species Generation and Aerobic 4-Chlorophenol Degradation, *Environmental Science & Technology*, 2017, **51**, 8101-8109.
4. Y. Shi, Z. Yang, L. Shi, H. Li, X. Liu, X. Zhang, J. Cheng, C. Liang, S. Cao, F. Guo, X. Liu, Z. Ai and L. Zhang, Surface Boronizing Can Weaken the Excitonic Effects of BiOBr Nanosheets for Efficient O₂ Activation and Selective NO Oxidation under Visible Light Irradiation, *Environmental Science & Technology*, 2022, **56**, 14478-14486.
5. P. J. Stephens, F. J. Devlin, C. F. Chabalowski and M. J. Frisch, Ab Initio Calculation of Vibrational Absorption and Circular Dichroism Spectra Using Density Functional Force Fields, *The Journal of Physical Chemistry*, 1994, **98**, 11623-11627.
6. L. Qin, H. Ye, C. Lai, S. Liu, X. Zhou, F. Qin, D. Ma, B. Long, Y. Sun, L. Tang, M. Yan, W. Chen, W. Chen and L. Xiang, Citrate-regulated synthesis of hydrotalcite-like compounds as peroxymonosulfate activator - Investigation of oxygen vacancies and degradation pathways by combining DFT, *Applied Catalysis B: Environmental*, 2022, **317**.
7. Z.-H. Xie, C.-S. He, Y.-L. He, S.-R. Yang, S.-Y. Yu, Z. Xiong, Y. Du, Y. Liu, Z.-C. Pan, G. Yao and B. Lai, Peracetic acid activation via the synergic effect of Co and Fe in CoFe-LDH for efficient degradation of pharmaceuticals in hospital wastewater, *Water Research*, 2023, **232**, 119666.
8. H. Lee, H.-J. Lee, J. Seo, H.-E. Kim, Y. K. Shin, J.-H. Kim and C. Lee, Activation of Oxygen and Hydrogen Peroxide by Copper(II) Coupled with Hydroxylamine for Oxidation of Organic Contaminants, *Environmental Science & Technology*, 2016, **50**, 8231-8238.
9. H. Li, R. Qiu, Y. Tang, X. Duan, Y. Gu, H. Yang, Q. Chen, Z. Shu, L. Xiang, S. Liu and X. Tan, Formation of Fe(IV) over a wide pH range via iron-carbon composite-catalyzed persulfate activation, *Chemical Engineering Journal*, 2023, **461**.
10. C. R. Keenan and D. L. Sedlak, Factors Affecting the Yield of Oxidants from the Reaction of Nanoparticulate Zero-Valent Iron and Oxygen, *Environmental Science & Technology*, 2008, **42**, 1262-1267.
11. Z. Wang, J. Jiang, S. Pang, Y. Zhou, C. Guan, Y. Gao, J. Li, Y. Yang, W. Qiu and C. Jiang, Is Sulfate Radical Really Generated from Peroxydisulfate Activated by Iron(II) for Environmental Decontamination?, *Environmental Science & Technology*, 2018, **52**, 11276-11284.
12. T. T. M. Nguyen, H.-J. Park, J. Y. Kim, H.-E. Kim, H. Lee, J. Yoon and C. Lee, Microbial Inactivation by Cupric Ion in Combination with H₂O₂: Role of Reactive Oxidants, *Environmental Science & Technology*, 2013, **47**, 13661-13667.
13. Z. Yang, Y. Liu and J. Wang, MOF-derived Cu₀/C activation of molecular oxygen for efficient degradation of sulfamethazine, *Chemical Engineering Journal*, 2022, **427**.

14. L. Xu, L. Zhao, Y. Mao, Z. Zhou and D. Wu, Enhancing the degradation of bisphenol A by dioxygen activation using bimetallic Cu/Fe@zeolite: Critical role of Cu(I) and superoxide radical, *Separation and Purification Technology*, 2020, **253**, 117550.
15. H. Jin, L. Li, N. Luo, H. Niu, J. Han, L. Xu, Z. Hao, D. Cao and Y. Cai, Biochars-Fe PCu hybrides deriving from solid waste and waste acids for elimination of refractory organic pollutants from pharmaceutical wastewater, *Chemical Engineering Journal*, 2023, **465**.
16. S. Dong, C. Liu and Y. Chen, Boosting exciton dissociation and molecular oxygen activation by in-plane grafting nitrogen-doped carbon nanosheets to graphitic carbon nitride for enhanced photocatalytic performance, *Journal of Colloid and Interface Science*, 2019, **553**, 59-70.
17. J. Liu, K. Luo, X. Li, Q. Yang, D. Wang, Y. Wu, Z. Chen, X. Huang, Z. Pi, W. Du and Z. Guan, The biochar-supported iron-copper bimetallic composite activating oxygen system for simultaneous adsorption and degradation of tetracycline, *Chemical Engineering Journal*, 2020, **402**.